Improved thermoelectric performance through double substitution in shandite-type mixed-metal sulphides

ACS APPLIED ENERGY MATERIALS

Cite This: ACS Appl. Energy Mater. XXXX, XXX, XXX−XXX

Forum Article

www.acsaem.org

Improved Thermoelectric Performance through Double Substitution in Shandite-Type Mixed-Metal Sulfides

Panagiotis Mangelis, Paz Vaqueiro, and Anthony V. Powell*

Department of Chemistry, University of Reading, Whiteknights, Reading RG6 6AD, United Kingdom

Supporting Information

ABSTRACT: Substitution of tin by indium in shandite-type phases, $A_3Sn_2S_2$ with mixed Co/Fe occupancy of the A-sites is used to tune the Fermi level within a region of the density of states in which there are sharp, narrow bands of predominantly metal d-character. Materials of general formula $Co_{2.5+x}Fe_{0.5-x}Sn_{2-y}In_yS_2$ (x = 0, 0.167; $0.0 \leq y \leq 0.7$) have been prepared by solid-state reaction and the products characterized by powder X-ray diffraction. Electrical-transport property data reveal that the progressive depopulation of the upper conduction band as tin is replaced by indium increases the electrical resistivity, and the weakly temperature-dependent $\rho(T)$ becomes more semiconducting in character. Concomitant changes in the negative Seebeck coefficient, the temperature dependence of which becomes increasingly linear, suggests the more highly substituted materials are n-type degenerate semiconductors. The power factors of the substituted phases, while increased, exhibit a weak temperature dependence. The observed reductions in thermal conductivity are principally due to reductions in the charge-carrier contribution on hole doping. A maximum figure-of-merit of $(ZT)_{max}$ = 0.29 is obtained for the composition $Co_{2.667}Fe_{0.333}Sn_{1.6}In_{0.4}S_2$ at 573 K: among the highest values for an n-type sulfide at this temperature.

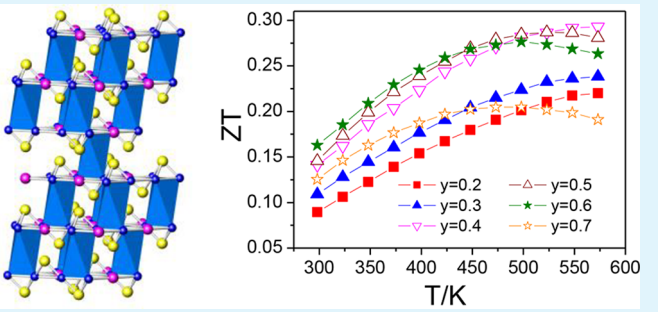

KEYWORDS: *thermoelectric, sulfide, shandite, electron transport, semiconductor, chalcogenide, thermal conductivity*

INTRODUCTION

The ability of thermoelectric devices to convert thermal energy directly into electrical energy offers considerable scope for improving the efficiency of industrial processes through the harvesting of waste heat. Device performance is determined principally by that of the constituent materials, commonly expressed in terms of a thermoelectric figure-of-merit, $ZT = S^2\sigma T/\kappa$ encompassing the Seebeck coefficient (S), electrical conductivity (σ), and thermal conductivity (κ), the last having contributions from lattice vibrations (κ_L) and charge carriers (κ_e).

Commercial thermoelectric devices are constructed from bismuth telluride, appropriately doped to produce the n- and p-type variants. However, the low abundance (1 ppb) and availability of tellurium[1,2] presents a barrier to the use of telluride-based devices in large-volume applications. Moreover, bismuth telluride exhibits its highest performance close to room temperature. Performance falls off at higher temperatures, making such devices unsuitable for applications at elevated temperatures, including the region $373 \leq T/K \leq 573$, where it has been estimated that ca. 80% of industrial waste heat is released.[3]

The search for new high-performance alternatives to bismuth telluride has led to the emergence of a number of design strategies. These include effecting reductions in thermal conductivity through the introduction of species with low-energy localized vibrational modes (the phonon−glass electron crystal (PGEC) approach),[4] the manipulation of interface scattering of phonons through grain-boundary engineering,[5] the introduction of nanoinclusions[6] or the formation of nanocomposites with a second phase,[7] or bringing about a liquid-like state of one sublattice in a crystalline material (the phonon−liquid electron crystal (PLEC) approach).[8] Similarly, electronic properties have been targeted through band structure modifications including the creation of resonant states,[9] energy filtering,[10] increasing the carrier effective mass through magnetic interactions,[11] enhancing the power factor through spin fluctuations of itinerant electrons,[12] or exploiting low dimensionality to enhance the Seebeck coefficient.[13]

Much of the recent interest in the development of alternatives to bismuth telluride has focused on sulfides due in part to the high abundance of sulfur (350,000 ppb).[1] A number of recent reviews[14−18] of sulfide thermoelectrics underline the significant advances achieved in p-type materials. Figures-of-merit which approach unity at elevated temperatures have been achieved in derivatives of tetrahedrite ($ZT \approx$

Special Issue: Thermoelectrics

Received: November 20, 2019
Accepted: December 3, 2019

DOI: 10.1021/acsaem.9b02272
ACS Appl. Energy Mater. XXXX, XXX, XXX−XXX

1.0 at 723 K)[19] and colusite ($ZT \approx 0.93$ at 675 K),[20] while the copper-deficient binary phases, $Cu_{2-x}S$ show even higher performance ($ZT = 1.7$ at 1000 K).[21]

Progress in n-type materials has generally been less marked. Compared to their p-type counterparts, the figures-of-merit of n-type materials are more modest. The n-type materials such as Bi_2S_3 ($ZT = 0.6$ at 760 K),[22] $MnBi_4S_7$ ($ZT = 0.21$ at 700 K),[23] and chalcopyrite-related phases ($ZT = 0.33$ at 700 K),[24] are among those with the highest figures-of-merit.

In the search for new n-type materials, we have sought to exploit the highly structured density of states $N(E)$ that result from low dimensionality in materials with the shandite structure. Shandite-type phases, $A_3M_2S_2$ (A = Ni, Co, Rh, Pd; M = Pb, In, Sn, Tl), adopt a structure[25] containing a kagome-like network of corner-sharing A_3 triangles, with M atoms located in sites of 6-fold coordination by A (Figure 1).

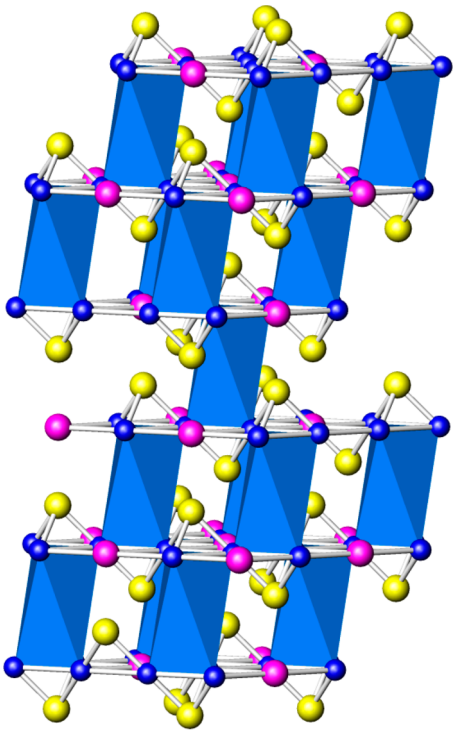

Figure 1. Shandite structure adopted by $Co_3Sn_2S_2$. Cobalt-centered trigonal antiprisms are shown as blue polyhedra; cobalt, tin, and sulfur atoms, as blue, magenta, and yellow circles.

Each A_3 triangle is capped by a sulfur atom. Additional M atoms are located in trigonal antiprismatic interlayer sites, linking kagome layers into a three-dimensional structure. In addition to fundamental studies to characterize the formal oxidation states in shandites,[26−29] materials in this family have attracted considerable interest for their electronic structure and properties[27,30−32] and magnetic properties[33−35] including the recent observation of more exotic phenomena such as Weyl semi-metal- and skyrmion-type behaviors.[36−39]

The low-dimensional character of the kagome layers is reflected in a density-of-states $N(E)$ that in the vicinity of the Fermi level, E_F, exhibits sharp, narrow bands, which band structure calculations reveal to be of predominantly Co d-character with small contributions from Sn 5p and S 3p states.[40] Since the Seebeck coefficient is proportional to the derivative of $N(E)$ at E_F, through the Mott relation,[41] tuning E_F to a sharp discontinuity in $N(E)$ may offer a means of increasing the Seebeck coefficient.[42] Indeed the resulting sharp peak in $N(E)$ of $Co_3Sn_2S_2$ at E_F may contribute to the relatively high Seebeck coefficient of the ternary phase.[43]

We have recently shown the applicability of such an approach by demonstrating that enhancements in thermoelectric performance can be realized by tuning E_F through the substitution of tin by indium in the series $Co_3Sn_{2-x}In_xS_2$.[44] This produces an almost 3-fold improvement in the room-temperature figure-of-merit in $Co_3Sn_{1.15}In_{0.85}S_2$ ($ZT = 0.2$) over that of the end-member phase $Co_3Sn_2S_2$.[40]

In a complementary approach to the tuning of electronic properties through manipulation of the position of E_F, we have explored chemical substitution at the transition-metal site (A-site).[45] While electron doping through nickel substitution in $Co_{3-x}Ni_xSn_2S_2$ ($0 \le x \le 3$) leads to loss of thermoelectric performance, as materials become more metallic, hole doping through the partial replacement of cobalt by iron in $Co_{3-x}Fe_xSn_2S_2$ ($0 \le x \le 0.6$) leads to performance enhancements. The power factor of $Co_{2.4}Fe_{0.6}Sn_2S_2$ reaches 10.3 μW cm^{-1} K^{-2} close to room temperature and $ZT = 0.2$ is achieved at 523 K in $Co_{2.6}Fe_{0.4}Sn_2S_2$. Given the comparative dearth of n-type sulfide thermoelectrics,[14] we have sought to achieve further enhancements in thermoelectric performance through substitution of tin by indium in n-type iron-substituted ($x \le 0.5$) phases, $Co_{3-x}Fe_xSn_{2-y}In_yS_2$. Here we report that this strategy results in n-type materials with figures-of-merit that approach $ZT = 0.3$ at temperatures in the critical $373 \le T/K \le 573$ region.

EXPERIMENTAL SECTION

Materials of composition $Co_{2.5+x}Fe_{0.5-x}Sn_{2-y}In_yS_2$ ($x = 0$, 0.167; $0.0 \le y \le 0.7$) were prepared by high-temperature synthesis from the powdered elements. Mixtures of cobalt (Alfa Aesar, powder, 99.8%), iron (Sigma-Aldrich, powder, 99.9%), tin (Sigma-Aldrich, powder, ≥99%), indium (350 mesh, Alfa, 99.99%), and sulfur (Sigma-Aldrich, flakes, 99.99%) of appropriate stoichiometry were ground in an agate pestle and mortar, prior to sealing into evacuated (10^{-4} mbar) fused-silica tubes. Mixtures were fired initially for 48 h at 773 K and subsequently, following an intermediate regrinding, at 973 K for a further 48 h. A heating/cooling rate of 0.5 K min^{-1} was used.

Powder X-ray diffraction data for the products were collected using a Bruker D8 Advance diffractometer, operating with Ge-monochromated Cu Kα_1 radiation ($\lambda = 1.5406$ Å) and equipped with a LynxEye linear detector. Diffraction data were collected over the angular range $10 \le 2\theta/° \le 120$, counting for 3.6 s at each increment of $2\theta = 0.018°$ in detector angle. Powder X-ray diffraction data were analyzed by the Rietveld method, as implemented in the General Structure Analysis System (GSAS) program.[46]

Powder samples were consolidated into pellets by hot pressing for 25 min in graphite molds at 973 K and 60 bar under a nitrogen atmosphere, using equipment constructed in-house. The resulting pellets have a diameter of ca. 12.7 mm and a thickness of ca. 2 mm. The density of the consolidated pellets was determined by the Archimedes method using an AE Adam PW 184 balance. Densities in excess of 98% of the crystallographic value were achieved for all materials.

Electrical resistivity and Seebeck coefficient data were collected simultaneously using a Linseis LSR3-800 system. Data were collected in 10 K intervals over the temperature range $303 \le T/K \le 673$. A current of 100 mA was used for the four-probe resistivity measurements and a temperature gradient of 50 K applied for the determination of Seebeck coefficients. Thermal diffusivity data in the temperature range $300 \le T/K \le 575$ were obtained using a Netzsch LFA 447 Nanoflash instrument. Data were collected in 25 K increments on circular pellets coated with graphite. The thermal

DOI: 10.1021/acsaem.9b02272
ACS Appl. Energy Mater. XXXX, XXX, XXX−XXX

conductivity was calculated using values of the heat capacity (0.365–0.368 J g^{-1} K^{-1}, depending on composition) obtained by application of the Dulong–Petit law. A recent round-robin exercise suggests uncertainties in measured resistivities, Seebeck coefficients, and thermal conductivities of 8%, 6%, and 11%, respectively, leading to a 19% uncertainty in ZT.[47]

RESULTS AND DISCUSSION

Powder X-ray diffraction data for compositions $Co_{2.5}Fe_{0.5}Sn_{2-y}In_yS_2$ reveal that the shandite structure is adopted throughout the composition range $0 \le y \le 0.6$. Similar behavior is observed in materials with higher cobalt content, $Co_{2.667}Fe_{0.333}Sn_{2-y}In_yS_2$, over the composition range $0.0 \le y \le 0.7$. The previously refined structures of the corresponding indium-free materials $Co_{2.5+x}Fe_{0.5-x}Sn_2S_2$ (x = 0.0, 0.2)[45] were used to provide the initial structural models for $Co_{2.5+x}Fe_{0.5}Sn_{2-y}In_yS_2$ phases, described in the space group $R\bar{3}m$. Similar atomic numbers of tin and indium prevent discrimination between these two elements by X-ray methods. However, a previous investigation of $Co_2Sn_{2-y}In_yS_2$ ($0 \le y \le 2$) by neutron diffraction and DFT has revealed that indium shows a preference for trigonal prismatic, interlayer sites over those in the kagome layer.[40] Site occupancy factors for the two main-group elements were therefore set according to the corresponding distribution in the iron-free materials. Thermal parameters of all elements were constrained to be equivalent and site occupancy factors fixed at those corresponding to the nominal compositions. Refinement proceeded smoothly, resulting in R_{wp} values of 2.8–3.1% and χ^2 in the range 1.26–1.47. Representative profiles appear in Figure 2, with the remaining provided as Supporting Information, while final refined parameters are presented in Table 1.

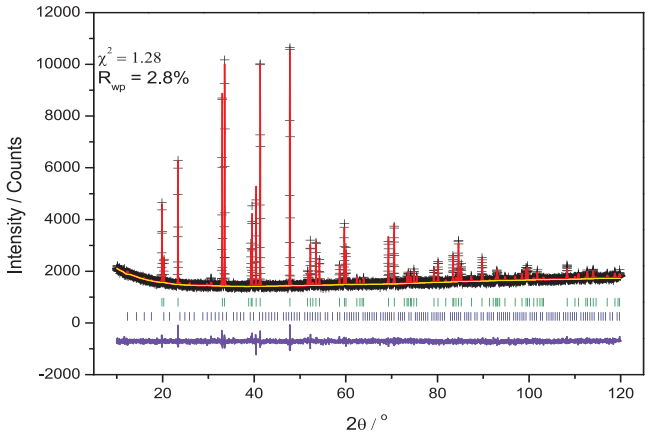

Figure 2. Final observed (crosses), calculated (full line), and difference (lower full line) X-ray profiles for $Co_{2.667}Fe_{0.333}Sn_{1.4}In_{0.6}S_2$. Reflection positions for the shandite phase are indicated by the upper set of vertical markers, while the lower set of markers refers to the $SnIn_4S_4$ impurity phase (ca. 4.4 wt %).

The compositional dependence of the lattice parameters of the two series of materials, $Co_{2.5+x}Fe_{0.5-x}Sn_{2-y}In_yS_2$ (x = 0.0, 0.133) is similar (Figure 3). In particular, the crystallographic c-parameter increases with increasing indium content, corresponding to an increase in the separation between kagome layers, while the in-plane a-parameter decreases slightly. An in-plane contraction on hole doping has been attributed to electronic factors, arising from the depopulation of antibonding states of predominantly d_{xy} and $d_{x^2-y^2}$ character in the vicinity of the Fermi level.[40]

The introduction of holes through the substitution of tin by indium increases the electrical resistivity for both series (Figures 4 and 5) as the upper conduction band is progressively depopulated. With increasing indium content, the weak temperature dependence of $\rho(T)$ at y = 0.0, for which $d\rho/dT$ is positive, is progressively transformed to temperature-dependent, semiconducting $\rho(T)$ behavior ($d\rho/dT$ negative). The resistivity at room temperature is increased by a factor of more than three across the series, with cobalt contents corresponding to x = 0.0, and by a similar factor for the series with x = 0.133.

The Seebeck coefficient (Figures 4 and 5) is negative for all compositions investigated, consistent with the dominant charge carriers being electrons. These materials therefore provide a comparatively rare example of an n-type sulfide. The absolute value of the Seebeck coefficient, $|S|$, increases with increasing indium content in both series investigated, consistent with the gradual loss of metallic behavior on substitution of tin with indium. Moreover, the $S(T)$ dependence becomes increasingly linear with increasing indium content, suggesting the more heavily substituted materials are degenerate semiconductors.

The power factors ($S^2\sigma$) of the indium-containing phases (Figure 6) exhibit a relatively weak temperature dependence, which contrasts with the behavior of indium-free $(Co,Fe)_3Sn_2S_2$ phases.[45] For example, the power factor for $Co_{2.5}Fe_{0.5}Sn_{1.8}In_{0.2}S_2$ shows a maximum variation of ca. 1.3 μW cm^{-1} K^{-2} over the whole of the temperature range investigated: the variation in the more cobalt-rich phase $Co_{2.667}Fe_{0.333}Sn_{1.7}In_{0.3}S_2$, being similar. In both series, the power factor initially increases with indium substitution before decreasing at higher indium contents, suggesting there is an optimum carrier concentration. Efforts to measure the carrier concentration by Hall effect measurements were hampered by difficulties in obtaining suitable contacts.

The thermal conductivity of materials of general formula $Co_{2.5}Fe_{0.5}Sn_{2-y}In_yS_2$ ($0.0 \le y \le 0.6$) decreases with indium substitution (Figure 7), although, at the highest temperatures, the thermal conductivity of all phases tends toward a common value of 3.5–3.6 W m^{-1} K^{-1}. The lowest thermal conductivity is attained at a composition with $0.5 \le y \le 0.6$. The series $Co_{2.667}Fe_{0.333}Sn_{2-y}In_yS_2$ ($0.0 < y \le 0.7$) shows a similar decrease in thermal conductivity with indium substitution (Figure 7), with the lowest values, of the order 3.0–3.1 W m^{-1} K^{-1}, occurring at compositions in the region $0.6 \le y \le 0.7$. Using the Wiedemann–Franz law (L_0 = 2.44 × 10^{-8} W Ω K^{-2}), the electronic contribution (κ_e) to the thermal conductivity was determined and the lattice contribution (κ_L) calculated as the difference ($\kappa - \kappa_e$). This demonstrates that the reduction in thermal conductivity that occurs across both series is principally due to the reduction in κ_e, with κ_L showing a much weaker compositional dependence (Figures S3 and S4). This is consistent with the expectation that little mass-fluctuation scattering will result from the replacement of tin with an element, indium, of similar atomic mass.

Combining the electrical-transport property data with the measured thermal conductivities enables calculation of the thermoelectric figure-of-merit, ZT (Figure 8). Hole doping in the series $Co_{2.5}Fe_{0.5}Sn_{2-y}In_yS_2$ leads to an increase in the figure-of-merit at temperatures below 500 K, with a maximum value of ZT = 0.23 being achieved for $Co_{2.5}Fe_{0.5}Sn_{1.6}In_{0.4}S_2$ at

DOI: 10.1021/acsaem.9b02272
ACS Appl. Energy Mater. XXXX, XXX, XXX–XXX

Table 1. Refined Parameters from Rietveld Analysis[a] of Powder X-ray Diffraction Data for (a) $Co_{2.667}Fe_{0.333}Sn_{2-y}In_yS_2$ ($0.2 \le y \le 0.7$) and (b) $Co_{2.5}Fe_{0.5}Sn_{2-y}In_yS_2$ ($0.2 \le y \le 0.6$)

y	a/Å	c/Å	V/Å^3	$S(z)$	U_{iso}/Å^2	R_{wp}/%	χ^2
			(a) $Co_{2.667}Fe_{0.333}Sn_{2-y}In_yS_2$				
0.2	5.35723(3)	13.2450(1)	329.203(5)	0.2833(3)	0.51(4)	3.0	1.41
0.3	5.35086(3)	13.2755(1)	329.17(1)	0.2828(3)	0.49(4)	2.8	1.25
0.4	5.34507(9)	13.3102(2)	329.32(1)	0.2829(3)	0.14(4)	3.0	1.26
0.5	5.33903(4)	13.3451(1)	329.441(6)	0.2820(3)	0.57(4)	3.0	1.37
0.6	5.33310(4)	13.3779(1)	329.516(6)	0.2819(3)	0.63(3)	2.8	1.28
0.7	5.32931(4)	13.4098(1)	329.833(6)	0.2817(3)	0.18(4)	3.1	1.47
			(b) $Co_{2.5}Fe_{0.5}Sn_{2-y}In_yS_2$				
0.2	5.35674(3)	13.2564(1)	329.424(5)	0.2831(3)	0.76(4)	2.8	1.29
0.4	5.34644(4)	13.3197(1)	329.727(6)	0.2832(3)	0.58(4)	2.9	1.26
0.5	5.33952(8)	13.3538(2)	329.72(1)	0.2816(3)	0.62(4)	3.0	1.26
0.6	5.33508(4)	13.3930(1)	330.133(6)	0.2821(3)	0.30(4)	3.1	1.42

[a]Space group: $R\bar{3}m$. Co/Fe on 9*d* (1/2,0,1/2), Sn(1) on 3*a*(0,0,0), Sn(2) on 3*b* (0,0,1/2), and S on 6*c* (0,0,*z*).

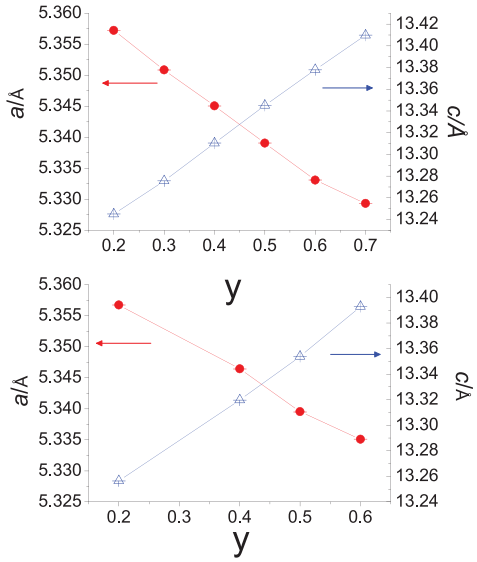

Figure 3. Compositional variation of the lattice parameters of $Co_{2.667}Fe_{0.333}Sn_{2-y}In_yS_2$ (upper plot) and $Co_{2.5}Fe_{0.5}Sn_{2-y}In_yS_2$ (lower plot), determined from Rietveld analysis of powder X-ray diffraction data at room temperature.

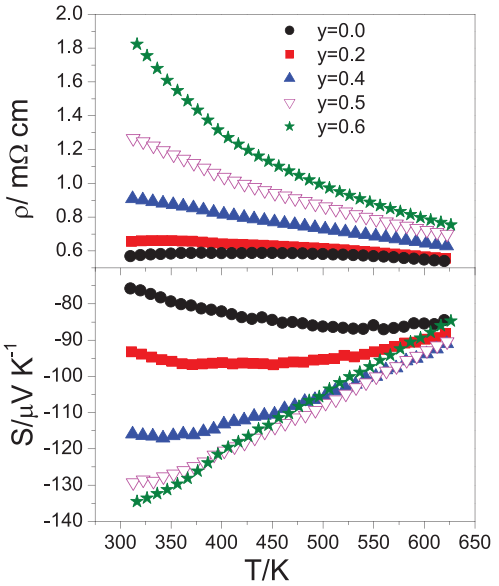

Figure 4. Temperature dependence of electrical resistivity (upper plot) and Seebeck coefficient (lower plot) of $Co_{2.5}Fe_{0.5}Sn_{2-y}In_yS_2$ phases ($0.0 \le y \le 0.6$).

500 K. This can be associated principally with the improvement in power factor since the thermal conductivity of this substituted phase (3.35 W m^{-1} K^{-1}) is comparable with that of the indium-free end-member (3.45 W m^{-1} K^{-1}) at this temperature.

Slightly greater enhancements in the figure-of-merit are observed in the series $Co_{2.667}Fe_{0.333}Sn_{2-y}In_yS_2$, with the maximum ZT = 0.29, being obtained for the composition $Co_{2.667}Fe_{0.333}Sn_{1.6}In_{0.4}S_2$ at 573 K. The compositional dependence of the figure-of-merit (Figure 8) mirrors that of the power factor, increasing gradually to y = 0.6, before an abrupt decrease at y = 0.7, due principally to the increase in electrical resistivity. The increase in the figure-of-merit up to compositions with y = 0.6 can be associated with the marked increase in the absolute value of the Seebeck coefficient that occurs with increasing hole concentration, while the increased electrical resistivity has a marked impact on κ_e, the reduction of which combines with the increase in power factor to raise ZT.

The partial replacement of cobalt by iron in the end-member phases $Co_{2.5}Fe_{0.5}Sn_2S_2$ and $Co_{2.667}Fe_{0.333}Sn_2S_2$ leads to the creation of holes and depopulation of the conduction band. The subsequent substitution of tin by indium, introduces additional holes. Therefore, the total hole content in the series $Co_{2.5+x}Fe_{0.5-x}Sn_{2-y}In_yS_2$ is given by $(0.5 - x) + y$. Comparison of the two nonstoichiometric series presented here reveals that the optimum figures-of-merit are exhibited by compositions corresponding to $(0.5 - x) + y$ in the range 0.7−0.9 holes per formula unit. In the previously reported series $Co_3Sn_{2-x}In_xS_2$ the maximum figure-of-merit in the temperature range $400 \le T/K \le 500$ occurs at x = 0.8. The parent phase, $Co_3Sn_2S_2$, has 47 valence electrons. Band structure calculations[31,40] reveal that the Fermi level crosses the narrow half-occupied 24th (conduction) band. Hole doping, through substitution, at either the transition-metal or main-group metal site, removes electrons from this band moving E_F toward the band edge, until at a level of 1 hole per formula unit, the 24th band is completely depopulated, E_F moves into the band gap, and the material becomes a semiconductor. Further doping can shift E_F into the lower energy 23rd valence band, leading to the re-emergence of a metal-like state.[44] A hole concentration of 0.7−0.9 positions E_F near the lower energy edge of the conduction band, where the high degree of curvature may be the origin of

DOI: 10.1021/acsaem.9b02272
ACS Appl. Energy Mater. XXXX, XXX, XXX−XXX

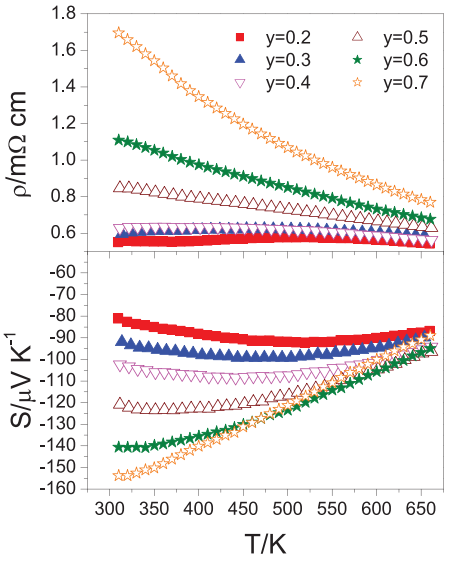

Figure 5. Temperature dependence of electrical resistivity (upper plot) and Seebeck coefficient (lower plot) of $Co_{2.667}Fe_{0.333}Sn_{2-y}In_yS_2$ phases ($0.2 \leq y \leq 0.7$).

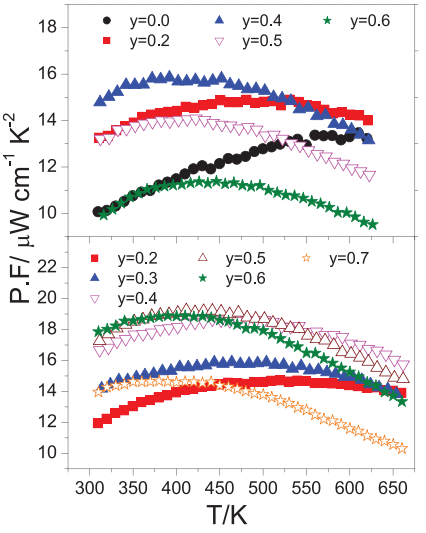

Figure 6. Thermoelectric power factors ($S^2\sigma$) for $Co_{2.5}Fe_{0.5}Sn_{2-y}In_yS_2$ ($0.0 \leq y \leq 0.6$, upper plot) and $Co_{2.667}Fe_{0.333}Sn_{2-y}In_yS_2$ phases ($0.2 \leq y \leq 0.7$, lower plot).

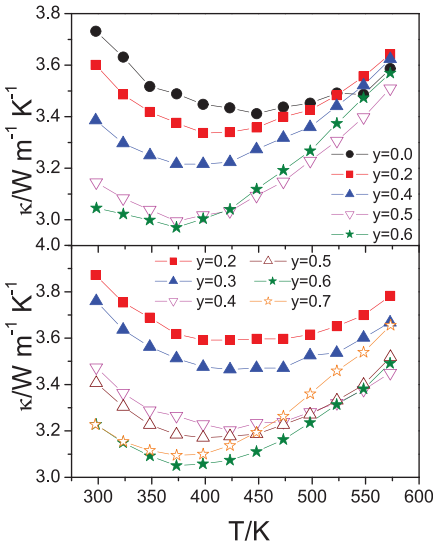

Figure 7. Temperature dependence of the total thermal conductivity (κ) of $Co_{2.5}Fe_{0.5}Sn_{2-y}In_yS_2$ phases ($0.0 \leq y \leq 0.6$, upper plot) and $Co_{2.667}Fe_{0.333}Sn_{2-y}In_yS_2$ phases ($0.2 \leq y \leq 0.7$, lower plot)

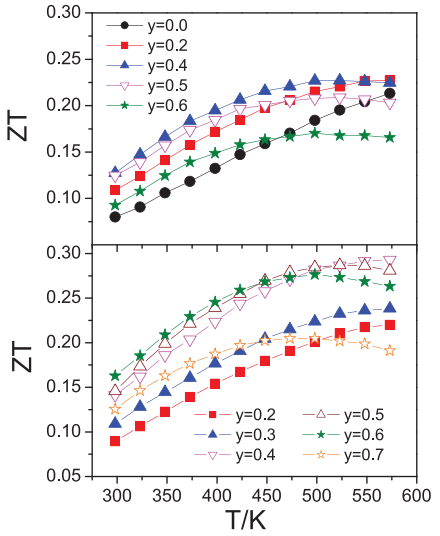

Figure 8. Temperature dependence of the thermoelectric figure-of-merit for $Co_{2.5}Fe_{0.5}Sn_{2-y}In_yS_2$ ($0.0 \leq y \leq 0.6$, upper plot) and $Co_{2.667}Fe_{0.333}Sn_{2-y}In_yS_2$ phases ($0.2 \leq y \leq 0.7$, lower plot).

the high Seebeck coefficient. Band structure calculations indicate that the conduction band is predominantly of d-character, with relatively little contribution from the p orbitals of the main-group metal.[40] The partial replacement of cobalt by iron may have an impact on the detailed form of this band and cause the critical region in which tuning of E_F optimizes the Seebeck coefficient to move to lower energies. The maximum thermoelectric response may then require a higher hole content in doubly substituted materials, than in materials where substitution is carried out at the main-group site only.

As noted above the performance of n-type materials lags behind that of their p-type counterparts, representing a barrier to construction of an all-sulfide thermoelectric device. For example, while Bi_2S_3, doped with $BiCl_3$, exhibits a maximum $ZT \approx 0.6$ at 760 K,[22] it shows a lower performance at temperatures in the region ($373 \leq T/K \leq 573$), appropriate to energy harvesting from waste heat associated with industrial processes ($ZT \approx 0.25$ at 473 K). Much of the focus on n-type sulfides has been directed toward phases related to chalcopyrite ($CuFeS_2$)[14] and attempts to optimize the carrier concentration through chemical substitution.[48,49] Figures-of-merit in the range of $0.1 \leq ZT \leq 0.2$ have been achieved at temperatures in the range $400 \leq T/K \leq 700$. While $ZT = 0.33$ has been reported for $Cu_{0.97}Fe_{1.03}S_2$,[24] this is at 700 K, significantly above the temperatures relevant to industrial waste heat. In the temperature range $373 \leq T/K \leq 573$, a figure-of-merit that approaches $ZT = 0.3$ in the shandite-related materials reported here, exceeds that of the majority of candidate n-type sulfides that have been explored (Figure 9). Materials derived from shandite may therefore offer an alternative n-type sulfide material for thermoelectric applications in the midrange of temperatures.

DOI: 10.1021/acsaem.9b02272
ACS Appl. Energy Mater. XXXX, XXX, XXX−XXX

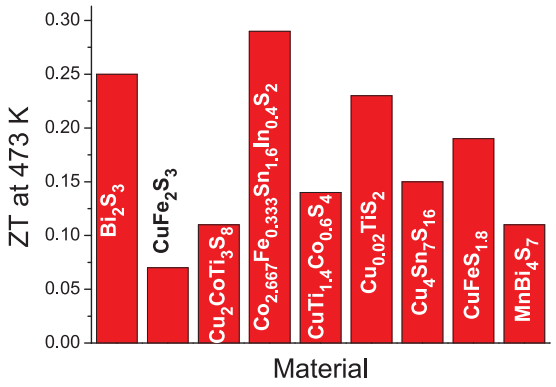

Figure 9. Comparison of the thermoelectric figure-of-merit of $Co_{2.667}Fe_{0.333}Sn_{1.6}In_{0.4}S_2$ at 473 K, the midpoint of the range at which the majority of industrial waste heat is released, with that of other candidate thermoelectric materials, Bi_2S_3,[22] $Cu_4Sn_7S_{16}$,[50] $Cu_{0.02}TiS_2$,[51] $CuTi_{1.4}Co_{0.6}S_4$,[52] $Cu_2CoTi_3S_8$,[53] $CuFe_2S_3$,[54] $CuFeS_{1.8}$,[55] and $MnBi_4S_7$.[23]

CONCLUSIONS

We demonstrate that hole doping through simultaneous substitution at the transition-metal and main-group metal atom site in $Co_3Sn_2S_2$ results in an increase in the thermoelectric figure-of-merit to a value that approaches ZT = 0.3 at temperatures as low as 473 K. Such materials are competitive with the more intensively investigated chalcopyrite-type and Bi_2S_3-type n-type phases. Materials such as $Co_{2.667}Fe_{0.333}Sn_{1.4}In_{0.6}S_2$ are therefore attractive candidates for further optimization of thermoelectric properties through techniques such as nanostructuring and nanocompositing to reduce the comparatively high thermal conductivity, without impacting unduly on the promising electrical properties.

ASSOCIATED CONTENT

Supporting Information

The Supporting Information is available free of charge at https://pubs.acs.org/doi/10.1021/acsaem.9b02272.

Final observed, calculated, and difference profiles from Rietveld analysis of powder X-ray diffraction data and electronic (κ_e) and lattice (κ_L) contributions to the thermal conductivity for both series (PDF)

AUTHOR INFORMATION

Corresponding Author

*E-mail: a.v.powell@reading.ac.uk.

ORCID

Panagiotis Mangelis: 0000-0001-5948-1177

Paz Vaqueiro: 0000-0001-7545-6262

Anthony V. Powell: 0000-0002-9650-1568

Funding

U.K. Engineering and Physical Sciences Council (Award Ref. 1367504).

Notes

The authors declare no competing financial interest.

ACKNOWLEDGMENTS

We thank EPSRC and the University of Reading for financial support for P.M. and for access to the Chemical Analysis Facility for powder X-ray diffraction measurements.

REFERENCES

(1) *CRC Handbook of Chemistry and Physics*, 87th ed.; Lide, D. R., Ed.; Taylor & Francis: Boca Raton, FL, USA, 2006.

(2) *U.S. Geological Survey, Mineral Commodity Summaries 2019*; U.S. Geological Survey: Reston, VA, USA, 2019; DOI: 10.3133/70202434.

(3) Kajikawa, T. Thermoelectric power generation system recovering industrial waste heat. In *Thermoelectrics Handbook: Macro to Nano*; Rowe, D. M., Ed.; CRC Press: Boca Raton, FL, USA, 2006; Chapter 50, pp 1−28.

(4) Slack, G. A. New materials and performance limits for thermoelectric cooling. In *CRC Handbook of Thermoelectrics*; Rowe, D. M., Ed.; CRC Press: Boca Raton, FL, USA, 1995; Chapter 34, pp 407−440.

(5) Kim, S. I. I.; Lee, K. H.; Mun, H. A.; Kim, H. S.; Hwang, S. W.; Roh, J. W.; Yang, D. J.; Shin, W. H.; Li, X. S.; Lee, Y. H.; Snyder, G. J.; Kim, S. W. Dense dislocation arrays embedded in grain boundaries for high-performance bulk thermoelectrics. *Science* **2015**, *348*, 109−114.

(6) Kanatzidis, M. G. Nanostructured thermoelectrics: The New Paradigm? *Chem. Mater.* **2010**, *22*, 648−659.

(7) Zhao, L. D.; Zhang, B. P.; Li, J. F.; Zhou, M.; Liu, W. S.; Liu, J. Thermoelectric and mechanical properties of nano-SiC-dispersed Bi_2Te_3 fabricated by mechanical alloying and spark plasma sintering. *J. Alloys Compd.* **2008**, *455*, 259−264.

(8) Liu, H.; Shi, X.; Xu, F.; Zhang, L.; Zhang, W.; Chen, L.; Li, Q.; Uher, C.; Day, T.; Snyder, G. J. Copper ion liquid-like thermoelectrics. *Nat. Mater.* **2012**, *11*, 422−425.

(9) Heremans, J. P.; Wiendlocha, B.; Chamoire, A. M. Resonant levels in bulk thermoelectric semiconductors. *Energy Environ. Sci.* **2012**, *5*, 5510−5530.

(10) Liu, B.; Hu, J.; Zhou, J.; Yang, R. Thermoelectric transport in nanocomposites. *Materials* **2017**, *10*, 418.

(11) Vaney, J.-B.; Aminorroaya Yamini, A.; Takaki, H.; Kobayashi, K.; Kobayashi, N.; Mori, T. Magnetism-mediated thermoelectric performance of the Cr-doped bismuth telluride tetradymite. *Mater. Today. Phys.* **2019**, *9*, 100090.

(12) Tsujii, N.; Nishide, A.; Hayakawa, J.; Mori, T. Observation of enhanced thermopower due to spin fluctuation in weak itinerant ferromagnet. *Sci. Adv.* **2019**, *5*, eaat5935.

(13) Hicks, L. D.; Dresselhaus, M. S. Thermoelectric figure of merit of a one-dimensional conductor. *Phys. Rev. B: Condens. Matter Mater. Phys.* **1993**, *47*, 16631−16634.

(14) Powell, A. V. Recent developments in earth-abundant copper-sulfide thermoelectric materials. *J. Appl. Phys.* **2019**, *126*, 100901.

(15) Powell, A. V.; Vaqueiro, P. Chalcogenide Thermoelectric Materials. In *Thermoelectric Materials and Devices*; Nandhakumar, I., White, N. M., Beeby, S., Eds.; Royal Society of Chemistry: Cambridge, U.K., 2017; Chapter 2, pages 27−59, DOI: 10.1039/9781782624042-00027.

(16) Suekuni, K.; Takabatake, T. Cu−S based synthetic minerals as efficient thermoelectric materials at medium temperatures. *APL Mater.* **2016**, *4*, 104503.

(17) Ge, Z.-H.; Zhao, L.-D.; Wu, D.; Liu, X.; Zhang, B.-P.; Li, J.-F.; He, J. Low-cost, abundant binary sulfides as promising thermoelectric materials. *Mater. Today* **2016**, *19*, 227−239.

(18) Hebert, S; Berthebaud, D; Daou, R; Breard, Y; Pelloquin, D; Guilmeau, E; Gascoin, F; Lebedev, O; Maignan, A Searching for new thermoelectric materials: some examples among oxides, sulphides and selenides. *J. Phys.: Condens. Matter* **2016**, *28*, No. 013001.

(19) Lu, X.; Morelli, D. T.; Xia, Y.; Ozolins, V. Increasing the thermoelectric figure of merit of tetrahedrites by co-doping with nickel and zinc. *Chem. Mater.* **2015**, *27*, 408−413.

(20) Bourges, C.; Bouyrie, Y.; Supka, A. R.; Al Rahal Al Orabi, R.; Lemoine, P.; Lebedev, O. I.; Ohta, M.; Suekuni, K.; Nassif, V.; Hardy, V.; Daou, R.; Miyazaki, Y.; Fornari, M.; Guilmeau, E. High-performance thermoelectric bulk colusite by process controlled structural disordering. *J. Am. Chem. Soc.* **2018**, *140*, 2186−2195.

DOI: 10.1021/acsaem.9b02272
ACS Appl. Energy Mater. XXXX, XXX, XXX−XXX

(21) He, Y.; Day, T.; Zhang, T.; Liu, H.; Shi, X.; Chen, L.; Snyder, G. J. High Thermoelectric Performance in Non-Toxic Earth-Abundant Copper Sulfide. *Adv. Mater.* **2014**, *26*, 3974−3978.
(22) Biswas, K.; Zhao, L.-D.; Kanatzidis, M. G. Tellurium-Free thermoelectric: The Anisotropic *n*-Type semiconductor Bi_2S_3. *Adv. Energy. Mater.* **2012**, *2*, 634−638.
(23) Labégorre, J.-B.; Virfeu, A.; Bourhim, A.; Willeman, H.; Barbier, T.; Appert, F.; Juraszek, J.; Malaman, B.; Huguenot, A.; Gautier, R.; Nassif, V.; Lemoine, P.; Prestipino, C.; Elkaim, E.; Pautrot-d'Alençon, L.; Le Mercier, T.; Maignan, A.; Al Rahal Al Orabi, R.; Guilmeau, E. XBi_4S_7 (X = Mn, Fe): new cost-efficient layered n-type thermoelectric sulfides with ultralow thermal conductivity. *Adv. Funct. Mater.* **2019**, *29*, 1904112.
(24) Li, Y.; Zhang, T.; Qin, Y.; Day, T.; Snyder, G. J.; Shi, X.; Chen, L. Thermoelectric transport properties of diamond-like $Cu_{1-x}Fe_{1+x}S_2$ tetrahedral compounds. *J. Appl. Phys.* **2014**, *116*, 203705.
(25) Range, K.-J.; Rau, F.; Zabel, M.; Paulus, H. Crystal structure of nickel tin sulfide (3/2/2), $Ni_3Sn_2S_2$. *Z. Kristallogr. - Cryst. Mater.* **1997**, *212*, 50.
(26) Gutlich, P.; Range, K. J.; Felser, C.; Schultz-Munzenberg, C.; Tremel, W.; Walcher, D.; Waldeck, M. The valence states of nickel, tin, and sulfur in the ternary chalcogenide $Ni_3Sn_2S_2$ - XPS, ^{61}Ni and ^{119}Sn Mössbauer investigations, and band structure calculations. *Angew. Chem., Int. Ed.* **1999**, *38*, 2381−2384.
(27) Rothballer, J.; Bachhuber, F.; Pielnhofer, F.; Schappacher, F. M.; Pöttgen, R.; Weihrich, R. Effect of In-Sn ordering on semiconducting properties in $InSnCo_3S_2$ - X-ray, ^{119}Sn Mössbauer Spectroscopy, and DFT Studies. *Eur. J. Inorg. Chem.* **2013**, *2013*, 248−255.
(28) Umetani, A.; Nagoshi, E.; Kubodera, T.; Matoba, M. Electronic and magnetic nature of shandite-type $A_2Co_3S_2$ (A = Sn, In). *Phys. B* **2008**, *403*, 1356−1358.
(29) Skinner, W. M.; Qian, G.; Buckley, A. N. Electronic environments in $Ni_3Pb_2S_2$ (shandite) and its initial oxidation in air. *J. Solid State Chem.* **2013**, *206*, 32−37.
(30) Anusca, I.; Schmid, A.; Peter, P.; Rothballer, J.; Pielnhofer, F.; Weihrich, R. Half antiperovskites: IV. Crystallographic and electronic structure investigations on $A_2Rh_3S_2$ (*A* = In, Sn, Tl, Pb, Bi). *Z. Anorg. Allg. Chem.* **2009**, *635*, 2410−2428.
(31) Weihrich, R.; Anusca, I. Half Antiperovskites. III - Crystallographic and electronic structure effects in $Sn_{2-x}In_xCo_3S_2$. *Z. Anorg. Allg. Chem.* **2006**, *632*, 1531−1537.
(32) Rothballer, J.; Bachhuber, F.; Rommel, S. M.; Söhnel, T.; Weihrich, R. Origin and effect of In-Sn ordering in $InSnCo_3S_2$: a neutron diffraction and DFT study. *RSC Adv.* **2014**, *4*, 42183−42189.
(33) Vaqueiro, P.; Sobany, G. G. A powder neutron diffraction study of the metallic ferromagnet $Co_3Sn_2S_2$. *Solid State Sci.* **2009**, *11*, 513−518.
(34) Yan, W. N.; Zhang, X.; Shi, Q.; Yu, X. Y.; Zhang, Z. Q.; Wang, Q.; Li, S.; Lei, H. C. Critical behavior of half-metallic ferromagnet $Co_3Sn_2S_2$. *Solid State Commun.* **2018**, *281*, 57−61.
(35) Schnelle, W.; Leithe-Jasper, A.; Rosner, H.; Schappacher, F. M.; Pottgen, R.; Pielnhofer, F.; Weihrich, R. Ferromagnetic ordering and half-metallic state of $Sn_2Co_3S_2$ with the shandite-type structure. *Phys. Rev. B: Condens. Matter Mater. Phys.* **2013**, *88*, 144404.
(36) Weihrich, R.; Pottgen, R.; Pielnhofer, F. From laboratory press to spins with giant effects. *Angew. Chem., Int. Ed.* **2018**, *57*, 15642−15644.
(37) Geishendorf, K.; Schlitz, R.; Vir, P.; Shekhar, C.; Felser, C.; Nielsch, K.; Goennenwein, S. T. B.; Thomas, A. Magnetoresistance and anomalous Hall effect in micro-ribbons of the magnetic Weyl semimetal $Co_3Sn_2S_2$. *Appl. Phys. Lett.* **2019**, *114*, No. 092403.
(38) Liu, E.; Sun, Y.; Kumar, N.; Muechler, L.; Sun, A.; Jiao, L.; Yang, S.-Y.; Liu, D.; Liang, A.; Xu, Q.; Kroder, J.; Süß; Borrmann, V. H.; Shekhar, C.; Wang, Z.; Xi, C.; Wang, W.; Schnelle, W.; Wirth, S.; Chen, Y.; Goennenwein, S. T. B.; Felser, C. Giant anomalous Hall effect in a ferromagnetic kagome-lattice semimetal. *Nat. Phys.* **2018**, *14*, 1125−1131.
(39) Wang, Q.; Xu, Q.; Lou, R.; Liu, Z.; Li, M.; Huang, Y.; Shen, D.; Weng, H.; Wang, S.; Lei, H. Large intrinsic anomalous Hall effect in half-metallic ferromagnet $Co_3Sn_2S_2$ with magnetic Weyl fermions. *Nat. Commun.* **2018**, *9*, 3681.
(40) Corps, J.; Vaqueiro, P.; Aziz, A.; Grau-Crespo, R.; Kockelmann, W.; Jumas, J.-C.; Powell, A. V. Interplay of metal-atom ordering, Fermi level tuning and thermoelectric properties in cobalt shandites $Co_3M_2S_2$ (M = Sn, In). *Chem. Mater.* **2015**, *27*, 3946−3956.
(41) Mott, N. F.; Davis, E. A. *Electronic processes in non-crystalline materials*. 2nd ed.; Oxford University Press: New York, 1979.
(42) Vaqueiro, P.; Powell, A. V. Recent developments in nanostructured materials for high-performance thermoelectrics. *J. Mater. Chem.* **2010**, *20*, 9577−9584.
(43) Dedkov, Y. S.; Holder, M.; Molodtsov, S. L.; Rosner, H. Electronic structure of shandite $Co_3Sn_2S_2$. *J. Phys.: Conf. Ser.* **2008**, *100*, No. 072011.
(44) Corps, J.; Vaqueiro, P.; Powell, A. V. $Co_3M_2S_2$ (M = Sn, In) Shandites as tellurium-free thermoelectrics. *J. Mater. Chem. A* **2013**, *1*, 6553−6557.
(45) Mangelis, P.; Vaqueiro, P.; Jumas, J.-C.; da Silva, I.; Smith, R. I.; Powell, A. V. The effect of electron and hole doping on the thermoelectric properties of shandite-type $Co_3Sn_2S_2$. *J. Solid State Chem.* **2017**, *251*, 204−210.
(46) Larson, A. C.; von Dreele, R. B. *General Structure Analysis System (GSAS)*, Los Alamos National Laboratory Report LAUR 86-748; Los Alamos National Laboratory: Los Alamos, NM, USA, 2004.
(47) Alleno, E.; Bérardan, D.; Byl, C.; Candolfi, C.; Daou, R.; Decourt, R.; Guilmeau, E.; Hébert, S.; Hejtmanek, J.; Lenoir, B.; Masschelein, P.; Ohorodnichuk, V.; Pollet, M.; Populoh, S.; Ravot, D.; Rouleau, O.; Soulier, M. A round robin test of the uncertainty on the measurement of the thermoelectric dimensionless figure of merit of $Co_{0.97}Ni_{0.03}Sb_3$. *Rev. Sci. Instrum.* **2015**, *86*, No. 011301.
(48) Tsujii, N.; Mori, T. High Thermoelectric power factor in a carrier-doped magnetic semiconductor $CuFeS_2$. *Appl. Phys. Express* **2013**, *6*, No. 043001.
(49) Tsujii, N.; Mori, T.; Isoda, Y. Phase stability and thermoelectric properties of $CuFeS_2$-based magnetic semiconductor. *J. Electron. Mater.* **2014**, *43*, 2371−2375.
(50) Bourgès, C.; Lemoine, P.; Lebedev, O. I.; Daou, R.; Hardy, V.; Malaman, B.; Guilmeau, E. Low thermal conductivity in ternary $Cu_4Sn_7S_{16}$ compound. *Acta Mater.* **2015**, *97*, 180−190.
(51) Guilmeau, E.; Bréard, Y.; Maignan, A. Transport and thermoelectric properties in copper intercalated TiS_2 chalcogenide. *Appl. Phys. Lett.* **2011**, *99*, No. 052107.
(52) Bourgès, C.; Pavan Kumar, V.; Nagai, H.; Miyazaki, Y.; Raveau, B.; Guilmeau, E. Role of cobalt for titanium substitution on the thermoelectric properties of the thiospinel $CuTi_2S_4$. *J. Alloys Compd.* **2019**, *781*, 1169−1174.
(53) Hashikuni, K.; Suekuni, K.; Watanabe, K.; Bouyrie, Y.; Ohta, M.; Ohtaki, M.; Takabatake, T. Carrier concentration tuning in thermoelectric thiospinel $Cu_2CoTi_3S_8$ by oxidative extraction of copper. *J. Solid State Chem.* **2018**, *259*, 5−10.
(54) Barbier, T.; Berthebaud, D.; Frésard, R.; Lebedev, O. I.; Guilmeau, E.; Eyert, V.; Maignan, A. Structural and thermoelectric properties of n-type isocubanite $CuFe_2S_3$. *Inorg. Chem. Front.* **2017**, *4*, 424−432.
(55) Li, J.; Tan, Q.; Li, J.-F. Synthesis and property evaluation of $CuFeS_{2-x}$ as earth-abundant and environmentally-friendly thermoelectric materials. *J. Alloys Compd.* **2013**, *551*, 143−149.

DOI: 10.1021/acsaem.9b02272
ACS Appl. Energy Mater. XXXX, XXX, XXX−XXX